ISSN 1070-3632, Russian Journal of General Chemistry, 2022, Vol. 92, No. 10, pp. 1995–2004. © Pleiades Publishing, Ltd., 2022.
Russian Text © The Author(s), 2022, published in Zhurnal Obshchei Khimii, 2022, Vol. 92, No. 10, pp. 1628–1639.

# Synthesis, Structure, and Spectral Properties of ZnTe-Containing Nanocomposites Based on Arabinogalactan

**M. V. Zvereva[a],* and A. V. Zhmurova[a]**

[a] *Favorskii Irkutsk Institute of Chemistry, Siberian Branch, Russian Academy of Sciences, Irkutsk, 664033 Russia*
**e-mail: mlesnichaya@mail.ru*

Received May 13, 2022; revised May 13, 2022; accepted June 10, 2022

**Abstract**—An environmentally friendly method of creating ZnTe-containing nanocomposites with varying amounts of inorganic phase (from 2.5 to 7.4%) using the stabilizing potential of the natural polysaccharide arabinogalactan and elemental tellurium was presented. A set of modern spectral, microscopic, and X-ray methods revealed that the obtained nanocomposites were formed as ZnTe nanoparticles of polycrystalline type, distributed in the polysaccharide matrix, with the size of 3–7 nm, the average diameter of 4.8 nm, and the stabilizing surface layer thickness of 18.7–37.7 nm. It was found that an increase in the zinc telluride content in the nanocomposites was accompanied by an increase in the hydrodynamic radius of the formed nanoparticles from 14 to 25 nm and from 47 to 70 nm for arabinogalactan–ZnTe nanocomposites with 2.5 and 7.4% ZnTe, respectively, as well as by a decrease in the optical band gap from 4.9 to 2.4 eV, respectively. This is probably due to an increase in size of the formed nanoparticles with increasing $Zn^{2+}/Te^{2-}$– arabinogalactan ratio.

**Keywords:** arabinogalactan, nanocomposites, nanoparticles, zinc telluride, polycrystals, quantum dots

**DOI:** 10.1134/S1070363222100139

Zinc telluride (ZnTe) is a representative of direct-gap inorganic semiconductors. Cubic ZnTe crystals provide an effective material for generating THz radiation by optical rectification, as well as for difference-frequency generation [1] and optical rectification applications [2]. ZnTe films are employed for detecting THz and gamma radiation and are used in electronic (LED, laser diodes) and optoelectronic (solar cells, photodetectors) devices [3]. When the dimensional characteristics of a material are reduced to the nanoscale, its properties are altered. For example, the thermal conductivity coefficient of ZnTe nanowires is lower than that of the crystals, which is essential for thermoelectric applications, since the thermoelectric figure of merit increases [4].

Development of synthesis methods for ZnTe-based semiconductor nanostructures (nanoparticles, quantum dots) is topical in view of the demand for their use in optoelectronics and photovoltaics [5], as well as in electrocatalysis [6] and medicine [7]. ZnTe nanoparticles exhibit pronounced antibacterial activity against drug-resistant *Escherichia coli* and *Vibrio cholerae* [7]. They can be used as low-toxic fluorescent labels as an alternative to labels with heavy metal-based quantum dots (CdX, PbX, X = $S^0$, $Se^0$, $Te^0$) [8].

Strict dependence of the biological, optical, thermoelectric, and other properties of nanoparticles on their morphological characteristics necessitates tuning the nanoparticles parameters in order to obtain nanomaterials with desired properties. With an increase in size of N-acetyl-L-cysteine-protected ZnTe nanoparticles from 2.88 to 3.06 nm, size-dependent bathochromic shift of the luminescence maximum from 509 to 550 nm was revealed [9]. A similar effect was observed in a study of the wavelength and intensity of the absorption and luminescence band maxima of ZnTe quantum dots as dependent on the synthesis conditions such as pH of the reaction medium, holding time, and type of passivating layer (thioglycol moieties or ZnSe shell in core–shell type quantum dots) on their surface [10]. The revealed dependences were associated with the size and the number of the produced ZnTe nanoparticles, as well as with formation of byproducts in the reaction and its redirection

toward production of ZnO rather than ZnTe nanoparticles in alkaline environment.

Biomedical applications require creation of water-soluble nanocomposites [11] able to afford strong biocompatibility. Such composites are obtained by chemical condensation methods employed for preparation of colloids. The main drawbacks of the known methods of synthesis of ZnTe nanoparticles are toxicity of the reactants and solvents used, as well as low eco-friendliness of the technology. Use of precursors such as highly toxic sodium borohydride, 2-sulfanylacetic acid, methanol, 2-sulfanylethanol, and metal salts, combined with long time (2–24 h) and high temperatures (100–150°C), result in an energy-intensive and environmentally unfriendly process.

When searching for new ways to synthesize ZnTe nanoparticles for biomedical applications one has to balance the goals of achievement of desired structural and photophysical characteristics (certain monodispersity of the nanoparticles, high photoluminescence quantum yield), compliance with medical requirements (good biocompatibility, water solubility, low toxicity, appropriate functionalization), and optimization of the synthesis route (implementation of green chemistry principles, short synthesis time, availability of chemicals, simple equipment).

Many of the above-mentioned tasks related to the synthesis of the ZnTe nanoparticles can be solved by using natural heteropolysaccharide arabinogalactan (AG) as a stabilizing ligand. Owing to its specific structure and unique properties (biocompatibility, water solubility, and intrinsic biological activity), this polysaccharide has successfully established itself as a reducing agent and stabilizer in the synthesis of polymer nanocomposites (with $Ag^0$, $Au^0$, $Pt^0$, $Pd^0$, $Fe_3O_4$, $Se^0$, $Te^0$ as an inorganic nano phase), possessing a set of biological, magnetic, catalytic, and optical properties [12, 13]. In synthesis of bismuth telluride nanoparticles, elemental tellurium powder served as a chalcogenide source [14]. Reactive chalcogenide anions were generated from elemental chalcogens in the $MOH–N_2H_4·H_2O$, M = Na, K reductive system, with absolutely eco-friendly $N_2$ and $H_2O$ being the only byproducts of the synthesis.

By carrying out the process in an aqueous medium with the use of arabinogalactan as a stabilizing matrix and elemental tellurium as a source of tellurium, not only targeted synthesis of water-soluble stable size-controlled ZnTe nanoparticles but also high eco-friendliness of the technology will be afforded. The resulting nanomaterials will potentially combine water solubility, stability, and biocompatibility due to arabinogalactan present in the composites with pronounced optical, thermoelectric, and antimicrobial properties due to the inorganic nano phase, ZnTe.

Herein, we present an efficient method for the synthesis and techniques for integrated characterization of the composition, structure, and properties of aggregatively stable water-soluble arabinogalactan–zinc telluride nanocomposites with the nanocore–shell structure, obtained for the first time. Formation of the water-soluble nanocomposites possessing aggregative stability in an aqueous medium was the result of the ion-exchange interaction of the zinc ions with the telluride anions preliminarily generated from elemental tellurium in the $NaOH–N_2H_4·H_2O$ alkaline reductive system. Telluride ion is highly reactive with oxygen and can only exist in an oxygen-free reaction medium at 60–70°C. Changes in conditions (lower temperature, air atmosphere, telluride ions added to solution of arabinogalactan in the absence of $Zn^{2+}$ ions) lead to rapid oxidation of $Te^{2-}$ ions to $Te^0$ and separation of tellurium from the reaction medium as a coarse precipitate. After adding an aliquot of the telluride anions to an aqueous solution of arabinogalactan and $Zn^{2+}$ ions, the reaction of ZnTe formation occurs instantaneously. Synthesis of the ZnTe nanoparticles in the arabinogalactan polysaccharide matrix is shown schematically in Fig. 1.

An increase in the concentration of the formed ZnTe molecules to a saturation threshold for the reaction medium leads to their stochastic aggregation via several reversible clustering events into tiny particles, solid phase nuclei. Further growth of the ZnTe particles occurs due presumably to the sequential coalescence of the ZnTe molecules on the surface of the growing nuclei, with possible merging of the nuclei with the nanoparticles. The arabinogalactan macromolecules passivate the produced ZnTe nanoparticles via adsorption on the zinc telluride surface and formation of a stabilizing layer, or via electrostatic interaction of the polar hydroxyl groups of arabinogalactan with noncompensated charges of $Zn^{2+}$ in the surface layer of the nanoparticles, or via both stabilization mechanisms combined.

According to the high-resolution transmission electron microscopy (HR-TEM) data, the arabinogalactan–zinc telluride nanocomposites are formed as nanoparticles distributed in the polysaccharide matrix, having a size

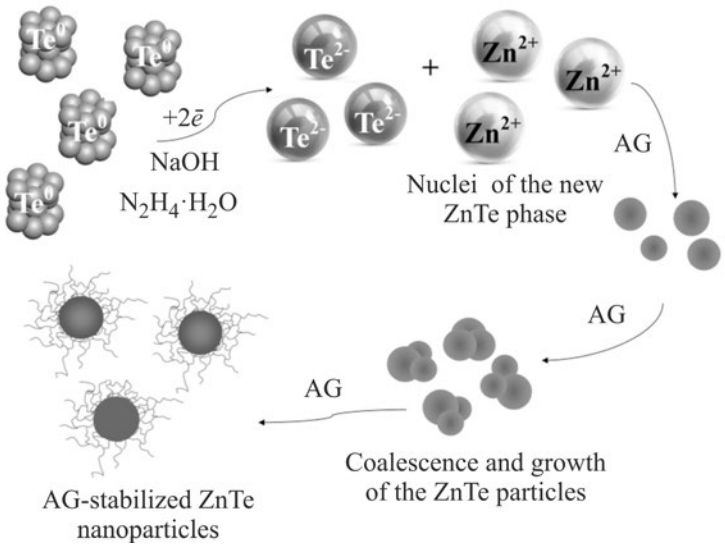


**Fig. 1.** Supposed scheme of the synthesis of the arabinogalactan (AG)-stabilized zinc telluride nanoparticles from elemental tellurium.

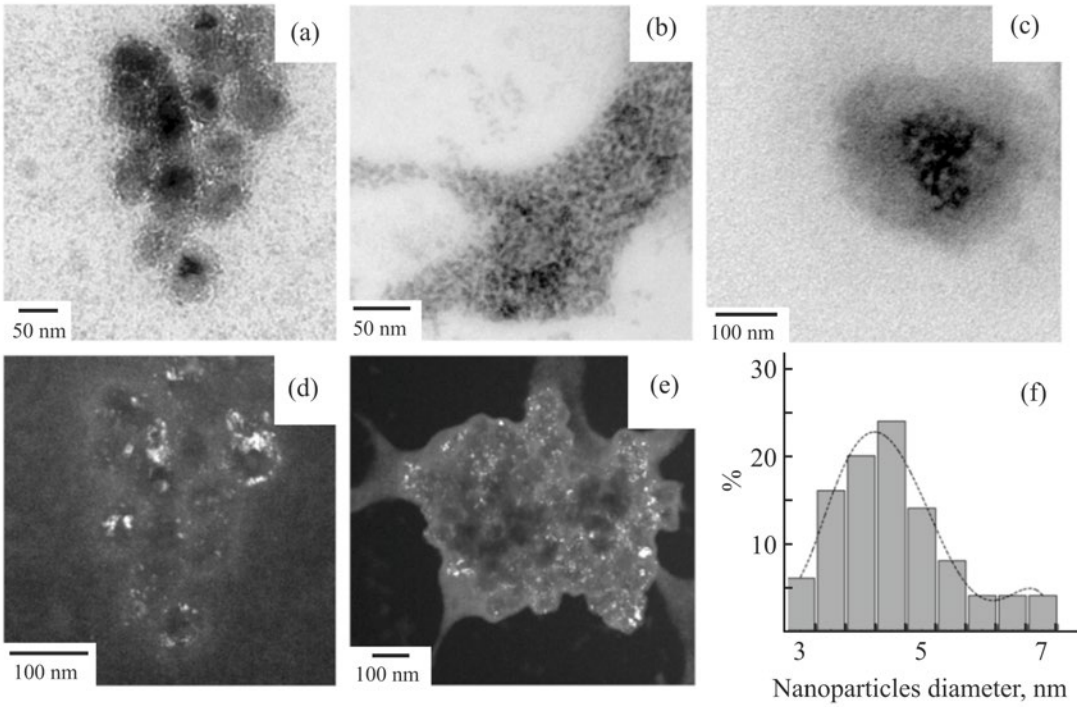


**Fig. 2.** (a–c) Bright-field and (d, e) dark-field microphotographs of the arabinogalactan–zinc telluride nanocomposite (2.5% ZnTe) and (f) size distribution diagram of the ZnTe nanoparticles in the arabinogalactan polysaccharide matrix.

of 3–7 nm and an average diameter of 4.8 nm (Figs. 2a and 2b). The particles form clusters of 21–47 nm size, surrounded by a polysaccharide shell (Fig. 2c). As shown by TEM examination, the shell thickness ranges within 18.7–37.7 nm.

By dark-field imaging, nanoparticles deviating from the spherical shape and contrasting strongly with the surrounding matrix are clearly visualized (Figs. 2d and 2e). The histogram in Fig. 2f shows close to normal positively skewed size distribution of the ZnTe

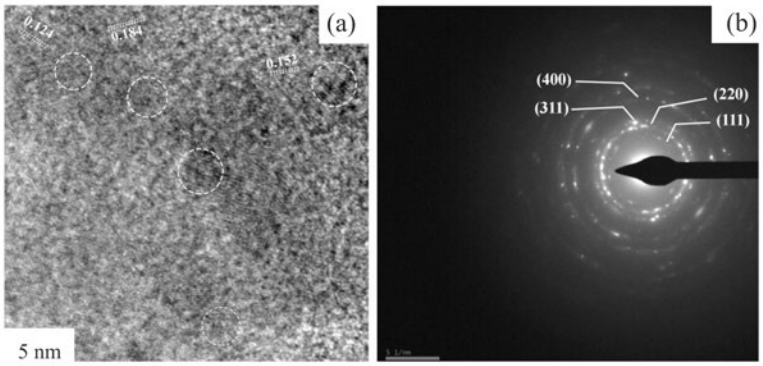


**Fig. 3.** (a) HR-TEM image of the arabinogalactan-stabilized zinc telluride nanoparticles with fringes appearing from diffraction on ZnTe planes and (b) electron diffraction pattern of the ZnTe nanoparticles.

nanoparticles in the composite, suggesting the growth and ripening of the ZnTe nanoparticles in the polysaccharide matrix occurring via successive attachment of the ZnTe molecules formed in the reaction medium to the surface of the growing nucleus, rather than via aggregation of the produced nanoparticles (this would have been evidenced by uniform particle size distribution).

Investigation of the internal microstructure of the nanoparticles by HR-TEM revealed inter-crossed fringes indicating the crystalline nature of the ZnTe nanoparticles (Fig. 3a); the inter-planar spacings between the adjacent lattice fringes (0.183, 0.152, and 0.124 nm) correspond to the crystal planes of zinc telluride (PDF #01-089-3054).

The selected area electron diffraction pattern of the ZnTe nanoparticles stabilized by the polysaccharide demonstrates clear and discrete reemission dots indicating good crystallinity of the nanoparticles (Fig. 3b). The electron diffraction pattern of the stabilized zinc telluride nanoparticles is represented by symmetrical rings with randomly distributed high-intensity contrast regions with no preferred orientation, suggesting its polycrystalline nature. Each identifiable dot on the rings arises from Bragg reflections from multiple crystals at different scattering angles, giving a continuous pattern of randomly oriented spots.

Dynamic light scattering (DLS) analysis of the aqueous solutions of the arabinogalactan-stabilized zinc telluride nanoparticles reveals multimodality of the scattering intensity-based particle size distribution (colloids consist of two or three fractions, Figs. 4b and 4c). In the aqueous solution of the nanocomposite sample (2.5% ZnTe), fractions of particles with hydrodynamic radii (*rh*) of 0.91, 14, and 47 nm were detected (Fig. 4b). Presumably, the first fraction of (fine) particles with *rh* of 0.91–1.2 nm is accounted for by individual arabinogalactan macromolecules occurring in the solution (*rh* 2.7 nm, Fig. 4a). The second and third fractions of particles (*rh* 14 and 47 nm) apparently represent agglomerates of the ZnTe nanoparticles formed in the arabinogalactan matrix, as detected in the TEM microphotographs.

The distribution based on the number of scattering particles is monomodal, with one fraction of fine (*rh* 0.91–1.12 nm) particles dominating in the solution. A probable reason for the lack of two other fractions of particles, corresponding to the polysaccharide-stabilized agglomerates and clusters of the ZnTe nanoparticles, is their negligible amount in the bulk of the sample analyzed. The observed pattern is almost identical to the particle size distribution of pure arabinogalactan, which reveals significant domination of the fraction of individual macromolecules adopting a coiled conformation in an aqueous solution over the fraction corresponding presumably to intermolecular associates of coil-like macromolecules (Fig. 4a).

As the content of the ZnTe nanoparticles in the nanocomposite increases, the fraction of fine particles completely disappears from its aqueous solution. The size distribution of the particles present in the aqueous solution of the nanocomposite sample (7.4% ZnTe) reveals fractions with *rh* of 25 and 70 nm. The lack of the fraction of fine particles, occurring in the solutions of the initial arabinogalactan or of the nanocomposite (2.5% ZnTe), is probably due to involvement of the free polysaccharide macromolecules in the mechanism of

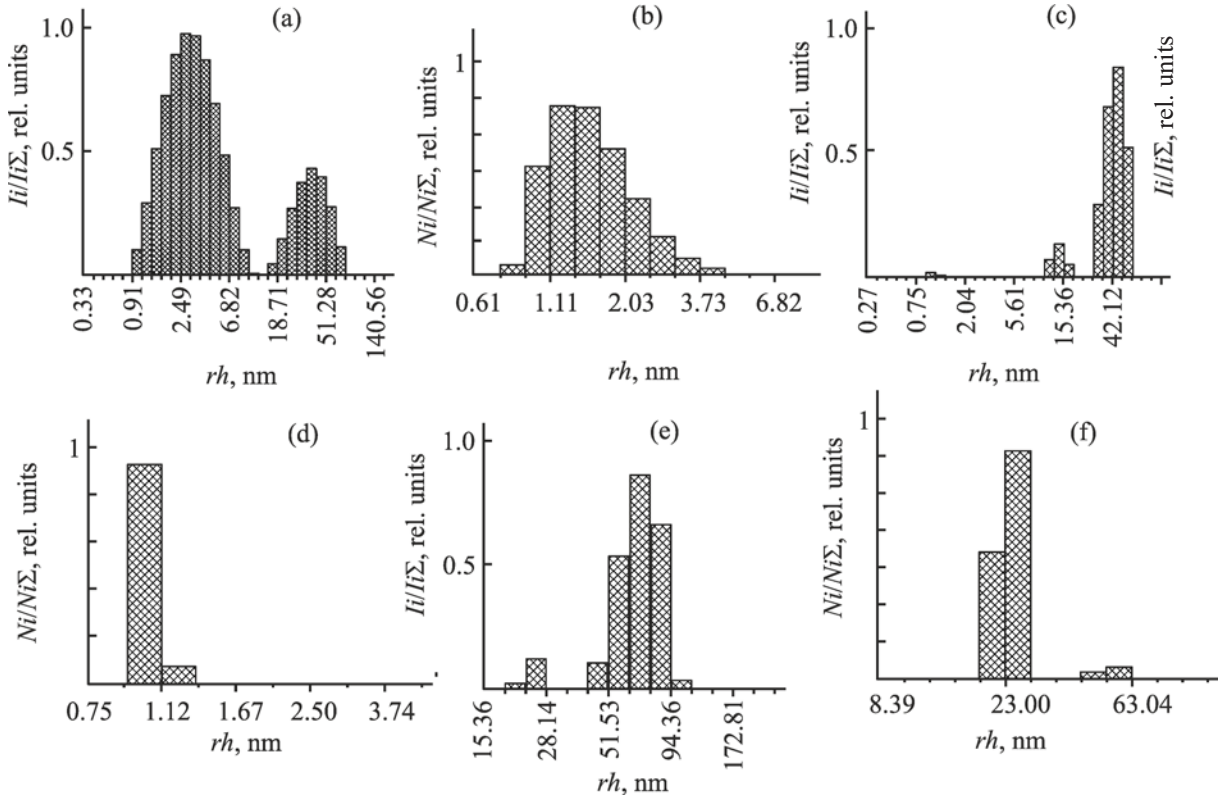


**Fig. 4.** Hydrodynamic radius (*rh*) distribution based on (a, c, e) light scattering intensity and (b, d, f) number of scattering particles for the samples of (a, b) initial arabinogalactan and (c–f) nanoparticles of arabinogalactan-stabilized zinc telluride (c, d) 2.5% ZnTe and (e, f) 7.4% ZnTe.

stabilization of the ZnTe nanoparticles. The average *rh* values for the fractions, characteristic of the stabilized nanoparticles, increase from 14 to 25 nm (2.5% ZnTe) and from 47 to 70 nm (7.4% ZnTe). The distribution based on the number of scattering particles is also bimodal (*rh* 25 and 57 nm), indicating reliably significant amount of scatters in the bulk of the analyzed solution.

For the nanocomposite sample (7.4% ZnTe), the influence of the ionic strength of the solution on its stability in aqueous solution was examined. The ζ-potential of the colloidal solution of the nanocomposite has negative values; for the solutions of the nanocomposite in the aqueous solutions of sodium chloride with NaCl concentrations of 0.01–0.05, 0.1, 0.2, and 0.5 g-eq/L the ζ-potential took the values of –24.4 to –12.3, –9.5, –3.4, –0.75, and –0.58 mV, respectively (Fig. 5). The observed decrease in the absolute value of the ζ-potential and, consequently, in stability of the arabinogalactan–ZnTe–$H_2O$ colloidal system in the solutions having high concentrations of singly charged ions is probably due to enhanced surface charge screening effect and a decrease in the Debye length, as well as to a decrease in thickness of the electrical double layer on the surface of the nanoparticles. All these factors cooperatively lead to coagulation, coarsening, and loss of sedimentation (kinetic) stability of the nanoparticles as accompanied by precipitation of the zinc telluride phase from the aqueous solution of the nanocomposite.

The ζ-potential and, accordingly, the stability of the aqueous solution of the nanocomposite are significantly affected by pH of the medium (Fig. 5b). The highest ζ-potential is exhibited by nanocomposite (7.4% ZnTe) at pH 8.0. A decrease in pH to 5.6, 2.8, 1.9, as well as an increase to 10.3 and 11.8, are accompanied by a decrease in the absolute value of the ζ-potential. Introduction of $H^+$ ions into the colloidal system with a negatively charged surface layer leads to partial neutralization of the negative charges and, consequently, to decreases in the absolute value of the ζ-potential and in stability of the system. Such dependence of the stability of a colloidal solution of

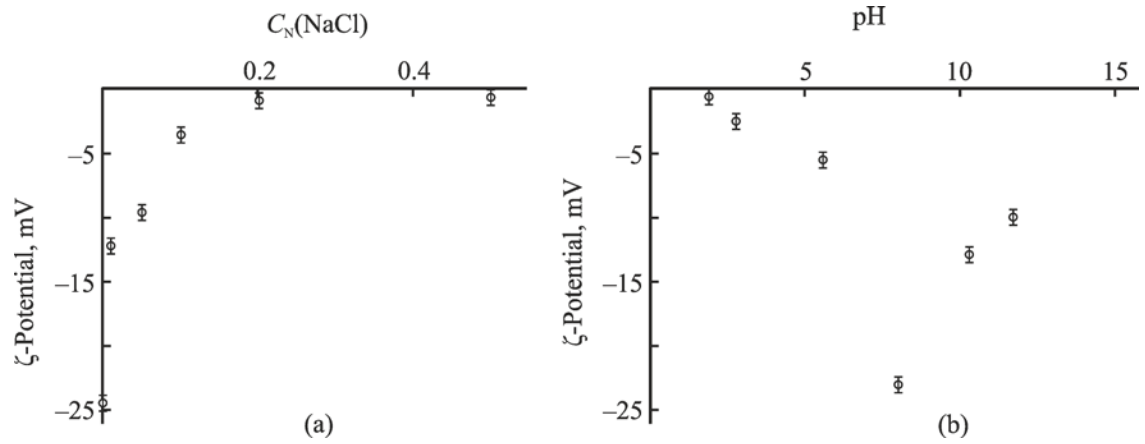


**Fig. 5.** ζ-potential of the solution of the arabinogalactan–zinc telluride nanocomposite (7.4% ZnTe) versus (a) electrolyte concentration and (b) pH of the medium.

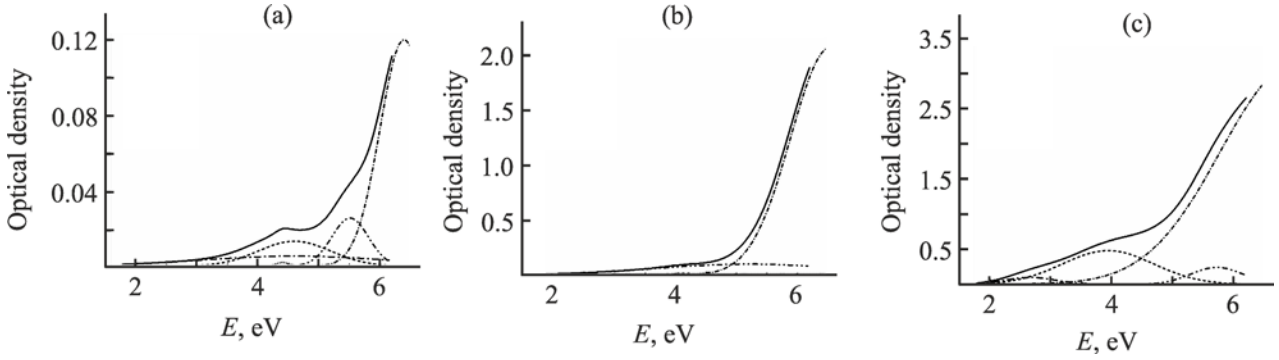


**Fig. 6.** Absorption spectra of (a) 0.2% aqueous solutions of arabinogalactan and (b, c) arabinogalactan–zinc telluride nanocomposite samples with (b) 2.5% ZnTe and (c) 7.4% ZnTe.

the polysaccharide-stabilized ZnTe nanoparticles on pH of their aqueous solutions may be associated with high sorption capacity of $H^+$ and $OH^-$ ions due to their small size ($H^+$) or high polarizability ($OH^-$).

In the electronic absorption spectra of 0.2% aqueous solutions of the nanocomposites, measured in the 200–600 nm range, a small absorption edge in the region of 217–237 nm (5.2–5.7 eV), as well as absorption in the region of 301–315 nm (3.9–4.1 eV), were revealed (Fig. 6). These low-resolution bands showed a blue shift with respect to the band at 548 nm (2.28 eV), corresponding to the optical band gap of the bulk ZnTe [15]. This shift is apparently due to quantum confinement observed in going from bulk-ZnTe particles to ZnTe nanoparticles whose radii are comparable to the Bohr radius, whereby the material acquires new properties dictated by the quantum size effect. The bands observed in the spectrum of arabinogalactan in the range of 4.4–5.5 eV (225–282 nm), which are due to the allowed n→σ* and the forbidden $n\rightarrow\pi^*$ transitions in the end aldehyde groups [16], as well as to absorption of microimpurities of natural flavonoids in arabinogalactan, are lacking in the absorption spectra of the nanocomposites, probably because of removal of impurities during synthesis, isolation, and purification of the nanocomposites [17]. An increase in the ZnTe amount in the nanocomposite from 2.5 to 7.4% and, accordingly, an increase in the nanoparticles size are accompanied by a bathochromic shift of the absorption band, λ 301–315 nm (3.93–4.12 eV), as well as by its growth in intensity and by improvement of its resolution, indicating the dependence on the nanoparticles size (Fig. 6).

The optical band gap of the stabilized ZnTe nanoparticles ($E_g$) was determined basing on the 10%

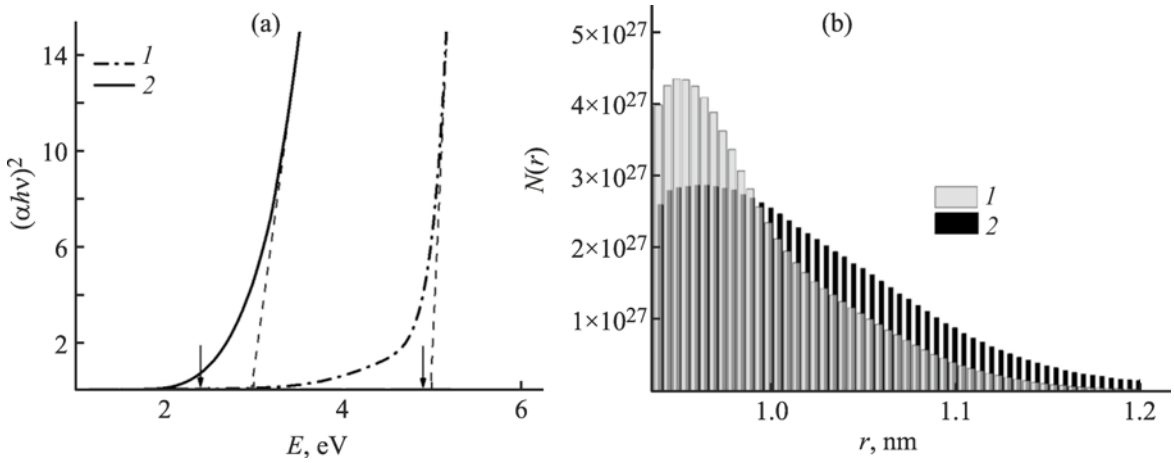


**Fig. 7.** (a) Spectral dependence of the absorption coefficient (presented as Tauc plot [19]) of arabinogalactan–zinc telluride nanocomposites and (b) size distribution of the nanoparticles in the nanocomposites with (*1*) 2.5% ZnTe and (*2*) 7.4% ZnTe, obtained by the method from [22]. Arrows indicate the optical band gap as determined basing on the 10% absorption peak height.

absorption peak height in the measured optical absorption spectrum of the nanocomposites of interest [18], as well as via extrapolation up to intersection with the abscissa-axis of linear parts experimental curves in the absorption spectra presented as Tauc plot [19] (Fig. 7a) in accordance with formula (1):

$$\alpha h\nu = A\left(h\nu - E_g\right)^{\gamma}. \quad (1)$$

Here, α is the absorption coefficient; $h\nu$, photon energy; $A$, an energy-independent constant; $E_g$, band gap energy; and γ, factor depending on the nature of the electron transition (γ = 1/2 for direct allowed transitions) [19].

Analysis of the data presented in Fig. 7a reveals a decrease in the optical band gap as determined by Tauc method [19] from 4.9 to 2.4 eV with an increase in the ZnTe amount in the nanocomposite from 2.5 to 7.4%. This is presumably due to an increase in the average size of the nanoparticles with an increase in the amount of inorganic phase in the arabinogalactan matrix. The obtained values exceed the optical band gap of bulk-ZnTe ($E_g^{bulk}$ 2.28 eV).

Such an increase in $E_g$ in going from bulk particles to nanoparticles (hypsochromic shift of $E_g$) is due to the presence of the quantum confinement effect. This effect appears when $r < r_B$, where r is the nanoparticle radius, and $r_B$, exciton Bohr radius [20]. For ZnTe with $r_B$ of 6.7 nm [21] this condition is satisfied, and thus, taking into account the r values determined by X-ray diffraction and TEM metods and considering nearly spherical shape of the nanoparticles, it is possible to estimate the average size of the formed ZnTe nanoparticles in the effective mass approximation (2) [21].

$$E_g = E_g^{bulk} + \frac{\hbar^2\pi^2}{2r^2}\left(\frac{1}{m_e} + \frac{1}{m_h}\right) - \frac{1.8e^2}{4\pi\varepsilon\varepsilon_0 r}. \quad (2)$$

Here, $E_g$ is the optical band gap of nanosized ZnTe; $E_g^{bulk}$ 2.28 eV, band gap of bulk ZnTe; ε 9.7, permittivity of bulk ZnTe; $m_h = m_h \cdot m_0 = 0.6m_0$, effective mass of the hole in ZnTe; $m_e = m_e \cdot m_0 = 0.13m_0$, effective mass of the electron in ZnTe; $m_0$, electron mass; $\hbar$, reduced Planck's constant; $r$, nanoparticle radius; $\varepsilon_0$, vacuum permittivity, and e, electron charge. The average diameter ($2r$) of the ZnTe nanoparticles was estimated by the Tauc method at 2.2 nm for the nanocomposite sample (2.5% ZnTe) and at 8.8 nm for the sample (7.4% ZnTe). To determine the most probable diameters of the nanoparticles in the nanocomposites, the corresponding size distributions were plotted according to the method from [22]. The latter allows determining the size distribution (3) in view of the established correlation between the nanoparticle size and the band gap shift (2) [21].

$$N(r) = -\frac{1}{V}\left[\frac{dD}{dr}\right] = -\frac{1}{\frac{4\pi r^3}{3}}\left[\frac{dD}{d\lambda}\frac{d\lambda}{dr}\right]\Bigg|_{\lambda=\frac{hc}{E_g(r)}}. \quad (3)$$

Here, $N(r)$ is the size distribution of the nanoparticles; $D$, optical density obtained by measuring the optical

absorption spectrum; $r$, radius of the nanoparticle; $V$, volume of the spherical nanoparticle; λ, wavelength; $E_g$, optical band gap of the nanosemiconductor; $h$, Planck's constant; and $c$, speed of light.

Figure 7b shows the monomodal lognormal distribution as calculated depending on the particle radius.

The most probable diameter of the nanoparticles in the nanocomposite slightly increases from 1.90 to 1.92 nm as the inorganic nano phase amount increases from 2.5 to 7.4%, and the shape of the histogram undergoes noticeable broadening in parallel with a decrease in the relative amount of the particles present at the distribution maximum. Our calculations of the size distribution according to the method from [22] gave correct qualitative as well as quantitative estimates of the most probable radii of the nanocomposite nanoparticles; specifically, they are of the same order of magnitude with the size characteristics determined by the TEM method and by using Eq. (2) from [21]. For the nanocomposite sample with 2.5% inorganic nano phase, the determined average nanoparticle diameter (based on TEM data), average diameter (according to Eq. (2) [21]), and most probable diameter of the nanoparticles [22] are 4.8, 2.2, and 1.9 nm, respectively.

Thus, using water-soluble polysaccharide arabinogalactan and the telluride anions generated from elemental tellurium powder by an eco-friendly route, we for the first time synthesized and characterized in detail arabinogalactan–zinc telluride nanocomposites (2.5–7.4% ZnTe). They are formed as quasispherical nanoparticles, exhibiting a pronounced tendency to form conglomerates, surrounded by a shell comprised of the polysaccharide macromolecules. The highest stability (ζ-potential of –24.4 mV) is displayed by the aqueous solutions of the nanocomposites with pH 7–8. An increase in the $Zn^{2+}/Te^{2-}$–arabinogalactan ratio taken for the synthesis of the nanocomposites is accompanied by increases in the average size of the resultant arabinogalactan-stabilized ZnTe particles and in their hydrodynamic radii, as well as by a decrease in the optical band gap from 4.9 to 2.4 eV. Our results suggest the possibility of targeted control of the size of the ZnTe nanoparticles being formed by varying the precursor ratio, as well as of the preparation of nanocomposite samples with desired physical, in particular, optical properties.

## EXPERIMENTAL

We used Siberian larch (*Larix Sibirica*) arabinogalactan, M 42.3 kDa (determined by size exclusion liquid chromatography [23]); elemental composition, %: C 41.9; H 7.4; O 50.7. Commercially available $Zn(NO_3)_2$, NaOH, ethanol (Reakhim), and tellurium powder (Sigma Aldrich) were used without further purification.

Microphotographs of the samples were recorded by the standard procedure on a FEI Tecnai G2 20F S-TWIN transmission electron microscope. For microscopic examination, a 2–3-mg weighed portion of the sample was dissolved in $H_2O$. The dilution was carried out until the optical density of the final solution was 0.1. Next, a drop of the resulting nanocomposite solution was placed on a support grid (Formvar/Carbon 200 Mesh, Copper, 50 p) and air-dried. The size distribution of the nanoparticles was determined by statistical processing of the microphotographs using the Digital Micrograph Software and Excel software package. The electron diffraction patterns obtained with the aid of the transmission electron microscope were processed using the ProcessDiffraction v.8.7.1 program, Crys TBox v.1.1 software, and the JCPDS-ICDD PDF-2 crystallographic database.

Elemental composition was determined by X-ray energy dispersive microanalysis on a Hitachi TM 3000 scanning electron microscope equipped with an SDD XFlash 430-4 X-ray detector and on a Thermo Scientific Flash 2000 CHNS analyzer. The hydrodynamic radius ($rh$) of the polysaccharide-stabilized ZnTe nanoparticles was determined by the dynamic light scattering (DLS) method on a Photocor Compact-Z photon correlation spectrometer (with a temperature stabilized semiconductor laser 638 nm, 20 mW, as a light source). The correlation function was analyzed with the use of the Dynals software for data processing in dynamic light scattering. The $rh$ values were calculated from the diffusion coefficients ($D$) by the Einstein–Stokes equation (4):

$$rh = kT/6\pi\eta_0 D. \quad (4)$$

Here, $\eta_0$ is the viscosity of the solvent; $k$, Boltzmann constant; and $T$, temperature. The particle size distribution was evaluated both by the standard procedure from the intensity of the scattered light by the particles and basing on the number of scattering particles. Solutions for the analysis were prepared by dissolving 5 mg of the sample for at least 7 h in 10 mL of distilled water, pre-filtered

through a syringe. The resulting solution was purified by filtration through a syringe filter (0.22 μm). The time of each measurement was at least 200 s. All measurements were made in triplicate.

The electrophoretic mobility of the nanoparticles was measured on a Photocor Compact-Z spectrometer using the PALS (Phase Analysis Light Scattering) protocol, which allows measuring the phase shift of an incident laser beam during light scattering caused by particle motion. Based on the obtained velocity of the particles in the field (calculated from the phase function), the electrophoretic mobility of the particles was determined:

$$\mu E = \nu/E, \quad (5)$$

where ν is the velocity of motion of charged particles in an electric field with strength $E$. The electrophoretic mobility $\mu E = \nu/E$ was converted to ζ-potential (the potential of a double electric layer on the particle surface) by means of the Smoluchowski equation (6):

$$\mu E = \varepsilon\varepsilon_0\zeta/\eta s, \quad (6)$$

where ε and $\varepsilon_0$ are the respective permittivities of the solvent and vacuum. All measurements were made in triplicate and averaged.

Absorption spectra of 0.2% aqueous solutions of the arabinogalactan–zinc telluride nanocomposites were recorded against distilled water in a 1-cm path length quartz cuvette in the wavelength range 190–1000 nm on a PerkinElmer Lambda 35 spectrophotometer.

**Telluride anions**. 0.7 mL of hydrazine hydrate was mixed with 0.05 g of NaOH, and the temperature of the resulting mixture was brought to 70°C with constant stirring. After the mixture was purged with argon, 0.08 g of tellurium powder was added, and the reaction mixture was stirred for 30 min in an argon atmosphere at 70°C until complete dissolution of tellurium. The resulting violet to red colored solution of the telluride anions was used for the preparation of the zinc telluride nanoparticles.

**Arabinogalactan–zinc telluride nanocomposites (2.5 ZnTe and 7.4% ZnTe)**. 0.264 (0.792) mmol of zinc nitrate was dissolved in 5 mL of ethylene glycol and added to 15 mL of 1.8% aqueous solution of arabinogalactan. The resulting mixture was kept for 15 min at 35°C until complete homogenization and uniform distribution of $Zn^{2+}$ ions in the reaction medium were achieved. Next, 20 or 140 μL of the solution of the telluride anions generated by the above-described procedure was added to the $Zn^{2+}$–arabinogalactan mixture and held at 35°C for 20 min. The nanocomposites were precipitated by adding a 4-fold excess of ethanol to the resulting mixture, filtered, washed with ethanol several times until neutral pH was reached, and dried in air. Yield 88–94%, dark gray amorphous powders, readily soluble in water. Nanocomposite sample (2.5% ZnTe). Found, %: C 42.2; H 7.2; O 48.1; Zn 0.7; Te 1.8. Nanocomposite sample (7.4% ZnTe). Found, %: C 39.7; H 5.6; O 47.3; Zn 2.4; Te 5.0.

## AUTHOR INFORMATION

M.V. Zvereva, ORCID: https://orcid.org/0000-0002-8385-3935

A.V. Zhmurova, ORCID: https://orcid.org/0000-0003-1804-1735

## FUNDING

This study was carried out under State Contract (project nos. 1021051703316-6-1.4.3, 121021000252-8) of the Basic Research Program of the Irkutsk Institute of Chemistry, Siberian Branch, Russian Academy of Sciences, using the equipment of the Baikal Analytical Center for Collective Use, Favorskii Irkutsk Institute of Chemistry, Siberian Branch, Russian Academy of Sciences, and of the Baikal Nanotechnology Center, Irkutsk National Research Technical University.

## CONFLICT OF INTEREST

No conflict of interest was declared by the authors.

## REFERENCES

1. Dadoenkova, Yu.S., Zolotovskii, I.O., Panyaev, I.S., and Sannikov, D.G., *Opt. Spectrosc*., 2018, vol. 124, no. 5, p. 712. https://doi.org/10.1134/S0030400X18050053
2. Guiramand, L., Ropagnol, X., and Blanchard, F., *Opt. Lett*., 2021, vol. 46, no. 24, p. 6047. https://doi.org/10.1364/OL.441231
3. Singh, H., Singh, T., and Sharma, J., *J. Micro Smart Syst*., 2018, vol. 7, no. 2, p. 123. https://doi.org/10.1007/s41683-018-0026-2
4. Davami, K., Weathers, A., Kheirabi, N., Mortazavi, B., Pettes, M.T., Shi, L., Lee, J.S., and Meyyappan, M., *J. Appl. Phys*., 2013, vol. 114, no. 13, p. 134314. https://doi.org/10.1063/1.4824687
5. El-Hachemi, B., Miloud, S., Sabah, M., Souad, T., Zineddine, O., Boubekeur, B., Toufik, S.M., and Ouahiba, H., *J. Inorg. Organomet. Polym. Mater*.,

2021, vol. 31, no. 9, p. 3637.
https://doi.org/10.1007/s10904-021-01994-3

6. Mollarasouli, F., Majidi, M.R., and Asadpour-Zeynali, K., *Int. J. Hydrogen Energ*., 2019, vol. 44, no. 39, p. 22085.
https://doi.org/10.1016/j.ijhydene.2019.06.071
7. Bu, H.B. and Kim, D., *Chem. Lett*., 2018, vol. 47, no. 2, p. 152.
https://doi.org/10.1246/cl.170917
8. Lincheneau, C., Amelia, M., Oszajca, M., Boccia, A., D'Orazi, F., Madrigale, M., Zanoni, R., Mazzaro, R., Ortolani, L., Morandi, V., Silvi, S., Szacilowski, K., and Credi, A., *J. Mater. Chem. C*, 2014, vol. 2, no. 16, p. 2877.
https://doi.org/10.1039/c3tc32385d
9. Ilanchezhiyan, P., Kumar, G.M., Xiao, F., Madhankumar, A., Siva, C., Yuldashev, S.U., Cho, H.D., and Kang, T.W., *Sol. Energy Mat. Sol. Cells*, 2018, vol. 183, p. 73.
https://doi.org/10.1016/j.solmat.2018.04.010
10. Cheng, T., Li, D., Li, J., Ren, B., Wang, G., and Cheng, J.W., *J. Mater. Sci: Mater. Electron*., 2015, vol. 26, no. 6, p. 4062.
https://doi.org/10.1007/s10854-015-2945-z
11. Xu, S.H., Wang, C.L., Xu, Q.Y., Zhang, H.S., Li, R.Q., Shao, H.B., Lei, W., and Cui, Y.P., *Chem. Mater*., 2010, vol. 22, no. 21, p. 5838.
https://doi.org/10.1021/cm101844j
12. Lesnichaya, M.V., Malysheva, S.F., Belogorlova, N.A., Graskova, I.A., Gazizova, A.V., Perfilyeva, A.I., Nozhkina, O.A., and Sukhov, B.V., *Russ. Chem. Bull*., 2019, vol. 68, no. 12, p. 2245.
https://doi.org/10.1007/s11172-019-2694-x.
13. Sosedova, L.M., Rukavishnikov, V.S., Sukhov, B.G., Borovskii, G.B., Titov, E.A., Novikov, M.A., Vokina, V.A., Yakimova, N.L., Lesnichaya, M.V., Kon'kova, T.V., Borovskaya, M.K., Graskova, I.A., Perfil'eva, A.L., and Trofimov, B.A., *Nanotechnol. Russ*., 2018, vol. 13, nos. 5–6, p. 290.
https://doi.org/10.1134/S1995078018030175
14. Lesnichaya, M.V., Zhmurova, A.V., and Sapozhnikov, A.N., *Russ. J. Gen. Chem.*, 2021, vol. 91, no. 7, p. 1379.
https://doi.org/10.1134/S1070363221070161
15. Madelung, O., in *Semiconductors: Data in Science and Technology*, Madelung, O., Ed., Berlin: Springer, 1992.
https://doi.org/10.1007/978-3-662-00464-7_3
16. Zhmurova, A.V., Zelenkov, L.E., Illarionov, A.I., Shendrik, R.Yu., Sapozhnikov, A.N., Klimenkov, I.V., Sukhov, B.G., and Trofimov, B.A., *Geogr. Nat. Resour*., 2016, no. 6, p. 169.
17. Lesnichaya, M.V., Shendrik, R.Y., Sapozhnikov, A.N., Sukhov, B.G., and Trofimov, B.A., *Russ. Chem. Bull*., 2017, vol. 66, no. 12, p. 2321.
https://doi.org/10.1007/s11172-017-2023-1
18. Wallace, A.M., Curiac, C., Delcamp, J.H., and Fortenberry, R.C., *J. Quant. Spectrosc. Rad. Transfer*., 2021, vol. 265, p. 107544.
https://doi.org/10.1016/j.jqsrt.2021.107544
19. Tauc, J., Grigorovici, R., and Vancu, A., *Phys. Stat. Sol*., 1966, vol. 15, no. 2, p. 627.
https://doi.org/10.1002/pssb.19660150224
20. Guzelturk, B., Martinez, P.L.H., Zhang, Q., Xiong, Q.H., Sun, H.D., Sun, X.W., Govorov, A.O., and Demir, H.V., *Laser Photon. Rev*., 2014, vol. 8, no. 1, p. 73.
https://doi.org/10.1002/lpor.201300024
21. Brus, L.E., *J. Chem. Phys*., 1984, vol. 80, no. 9, p. 4403.
https://doi.org/10.1063/1.447218
22. Pesika, N.S., Stebe, K.J., and Searson, P.C., *J. Phys. Chem. B*, 2003, vol. 107, no. 38, p. 10412.
https://doi.org/10.1021/jp0303218
23. Aleksandrova, G.P., Lesnichaya, M.V., Sukhov, B.G., Trofimov, B.A., and Boymirzaev, A.S., *Russ. J. Gen. Chem.*, 2015, vol. 85, no. 2, p. 490.
https://doi.org/10.1134/S107036321502022X